Modeling Flower Pigmentation Patterns

LEE RINGHAM, ANDREW OWENS, MIKOLAJ CIESLAK, LAWRENCE D. HARDER, and PRZEMYSLAW PRUSINKIEWICZ, University of Calgary, Canada

Fig. 1. A model and a photograph of a *Mimulus guttatus* flower. The comparison illustrates the degree of realism achievable by simulating known or biologically plausible patterning processes. Photograph by James Gaither, licensed under CC BY-NC-ND 2.0.

Although many simulation models of natural phenomena have been developed to date, little attention was given to a major contributor to the beauty of nature: the colorful patterns of flowers. We survey typical patterns and propose methods for simulating them inspired by the current understanding of the biology of floral patterning. The patterns are generated directly on geometric models of flowers, using different combinations of key mathematical models of morphogenesis: vascular patterning, positional information, reaction-diffusion, and random pattern generation. The integration of these models makes it possible to capture a wide range of the flower pigmentation patterns observed in nature.

Authors' address: Lee Ringham, laringha@ucalgary.ca; Andrew Owens, arowens@ucalgary.ca; Mikolaj Cieslak, msciesla@ucalgary.ca; Lawrence D. Harder, harder@ucalgary.ca; Przemyslaw Prusinkiewicz, pwp@ucalgary.ca, University of Calgary, 2500 University Dr. N.W., Calgary, AB, Canada, T2N 1N4.

1 INTRODUCTION

Modeling patterns of nature is an interesting and challenging endeavor. At the level of fundamental science, models can contribute to understanding the often non-intuitive processes of pattern emergence. As emergent phenomena are notoriously difficult to comprehend, each model is a mini-discovery, potentially complementing existing biological knowledge or becoming a hypothesis for biologists. From an image synthesis perspective, patterns generated directly on surfaces with the required geometry offer several advantages over texture mapping [Turk 1991]. The impact of light conditions on texture acquisition, and issues of distortion when mapping between surfaces with different geometries, are eliminated. Moreover, the generated patterns can be diversified by randomizing surface shapes, parameter values, initial conditions of the simulation, and/or by using stochastic simulation techniques, thus avoiding repetitions stemming from reusing the same scanned texture.

Here we present a method for generating flower pigmentation patterns. We begin by classifying patterns described in biological literature from the viewpoint of known or plausible patterning mechanisms. After identifying relatively simple patterns that have
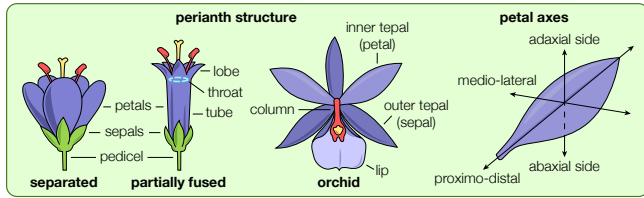
Fig. 2. Some biological terminology relevant to flower pigmentation patterns. The set of all petals is called the corolla, the set of sepals is the calyx, and the corolla and calyx jointly form the perianth. Based on [Sugden 1984].

been modeled before, and excluding outliers, we focus on four mechanisms that appear to underlie the remaining patterns: pigmentation driven by the vascular system, positional information, reaction-diffusion, and random pattern generation. We present computational models of these mechanisms and demonstrate, through a number of case studies, the astonishing diversity and complexity of patterns they can generate by acting alone or in combination. These case studies substantially extend the range and complexity of flower pigmentation patterns modeled to date.

From a technical perspective, the most complex element of our method is the simulation of anisotropic diffusion of pattern-inducing substances (morphogens [Turing 1952]) on a triangulated 2-manifold, taking into account the stochastic character of diffusion. Although each of these aspects of diffusion has been modeled previously, the integration of reported solutions is difficult because of their incompatible assumptions. For example, the method for simulating anisotropic diffusion on triangle meshes presented by Andreux et al. [2015] does not account for the stochastic character of diffusion, whereas the method for simulating stochastic reaction-diffusion presented by Ghosh et al. [2015] is limited to square grids. To provide a firm basis for simulations and clearly identify their parameters, we derived equations for anisotropic stochastic diffusion on triangle meshes from first principles. At the implementation level, our system makes it possible to interactively specify not only the parameters of the equations governing the simulations, but also the equations themselves, using a simple script. This capacity facilitates interactive development and exploration of models.

2 BACKGROUND

2.1 Biology of pigmentation

Colorful flowers evolve to attract animal pollinators — mainly insects and birds — and to guide them to specific locations within the flower [Willmer 2011]. Some flowers exhibit structural coloring due to the diffraction of light on the striated petal surface [Airoldi et al. 2019; Lee 2010], but the primary sources of colors are biological pigments [van der Kooi et al. 2016, 2014]. The most prominent of them are: anthocyanins, giving flowers hues ranging from blue to red, carotenoids (yellow, orange and red), and betalains (yellow and red) [Davies et al. 2012; Grotewold 2006; Lee 2010]. The biochemical pathways that synthesize these pigments are known and are believed to be similar across a wide range of plants [Albert et al. 2014a; Davies et al. 2012; Yamagishi 2013; Yuan et al. 2016]. In contrast, the mechanisms that regulate the spatial localization of

pigments, i.e., pigmentation patterns, are only partially understood [Davies et al. 2012; Yuan et al. 2016]. To comprehend the spectrum of flower pigmentation patterns, we have surveyed the patterning mechanisms described in the literature, and divided them into the following classes (see Fig. 2 for terminology):

(1) **Patterns associated with organ identity.** Examples include color variation between petals in bilaterally symmetric flowers (Fig. 3A), petals colored differently from sepals (Fig. 3B), and lips colored differently from the remaining elements of the perianth in orchids (Fig. 3C). These differences appear to be linked to genes controlling flower morphology [Davies et al. 2012].

(2) **Patterns associated with flower age.** Some flowers change color as they age. These changes produce color variation in inflorescences (flower clusters), in which flowers are produced sequentially (Fig. 3D).

(3) **Patterns associated with exposure to light.** An interesting phenomenon, termed bud blushing, is the pigmentation of the parts of petals exposed to light before the flower opens (Fig. 3E). Blushing may persist or gradually subside after the flower has opened.

(4) **Patterns associated with vasculature.** In many species, pigment distribution correlates with veins in petals or sepals [Shang et al. 2011] (Fig. 3, A and F).

(5) **Patterns associated with position within petals.** These patterns are characterized by the axis or axes along which pigmentation changes, and either the gradual (Fig. 3G) or discontinuous (Fig. 3H) character of this change. For example, the flower center may have a different color from the outer regions, petals may carry regular spots (Fig. 3I), and landmarks such as "landing platforms" directing pollinators to nectar or pollen may be colored differently from the surrounding areas (white area in Fig. 3J) [Davies et al. 2012].

(6) **Reaction-diffusion patterns.** Recent studies of flower pigmentation patterns in the monkeyflower genus *Mimulus* [Ding et al. 2020; Yuan et al. 2014] have shown that a prominent element of these patterns — dispersed spots — self-organize through a reaction-diffusion mechanism (Fig. 1). The visual character of many other patterns also suggests reaction-diffusion (e.g., Fig. 3, J and K).

(7) **Random patterns.** A striking example is provided by patterns that result from the random excision of transposable elements (transposons) from the genome of individual cells. This excision affects individual cells and their descendants (Fig. 3L) [Rolland-Lagan et al. 2003]. Random factors may also affect the outcome of other patterning mechanisms, for example, due to the stochastic character of biochemical processes at the molecular level.

The assignment of pigment colors to different organs or flowers of different age, characteristic of patterns in Class 1 and 2, is simple from a computer graphics perspective. The dependence of pigmentation on external conditions (light) distinguishes patterns in Class 3 from the remaining mechanisms. Consequently, in this paper we focus on mechanisms that can generate the patterns in classes 4–7.

Fig. 3. Examples of floral patterns. (A) Different coloring of petals in a bilaterally symmetric flower and patterning associated with veins: *Viola tricolor* (pansy); (B) Different coloring of petals (white and red) vs. sepals (red) in a radially symmetric flower: *Aquilegia* sp. (columbine); (C) Distinctive coloring of an orchid lip: *Cypripedium reginae*; (D) Color change from white to red as flowers age: *Onosma alborosea*; (E) Bud blushing: *Malus domestica* (apple); (F) Pigmentation associated with veins: *Oxalis adenophylla*; (G) Gradual color change along proximo-distal axis: *Plumeria alba* (frangipani); (H) Bicolor patterning: *Gaillardia aristata*; (I) Regular spots: *Wurmbea elatior*; (J) Irregular spots and a landing platform (white): *Galearis rotundifolia* (small round-leaved orchid); (K) Irregular blotches suggestive of a reaction-diffusion mechanism: *Fritillaria meleagris* (checkered lily); (L) Random pattern due to excision of transposons: *Antirrhinum majus* (snapdragon). Image (L) courtesy of Enrico Coen.

2.2 Computational models of morphogenesis

In spite of recent advances, biological understanding of flower pigmentation patterns is very incomplete. We thus complement biological knowledge with a repertoire of concepts rooted in theoretical studies of morphogenesis to develop specific models.

2.2.1 Canalization. A key factor in plant morphogenesis is the plant hormone auxin. Auxin-driven morphogenesis relies on feedback between concentrations or fluxes of auxin, and its subsequent transport. For example, in one variant of this process called facilitated diffusion, existing fluxes increase the further flow of auxin by locally increasing the diffusion coefficient (see [Cieslak et al. 2021] for a recent review). Sachs [2003] compared this mechanism to the formation of gullies when water flows down a sandy slope, and postulated that a similar mechanism patterns vascular strands in plants. In terms of fluid dynamics, auxin-driven patterning has been modeled both from the Eulerian perspective, with a focus on fluxes at different points of the underlying tissue, and from the Lagrangian perspective, with a focus on the motion of particles that represent auxin and that trace the vascular strands as they move [Cieslak et al. 2021]. We rely on this second perspective when procedurally generating petal veins.

2.2.2 Positional information. Wolpert [1969] proposed a model of morphogenesis based on the idea that cells have information about their position within tissues. This information is typically represented by concentrations of a morphogen diffusing from predefined sources to sinks. Gradual changes in morphogen concentrations are transformed into discrete patterns by thresholding. A canonical example is the "French flag problem", in which areas with high, medium and low levels of morphogen concentration are assigned three different colors [Wolpert 1969]. Conceptually, the positional information model may appear incomplete, for it relies on predefined positions of sources and sinks, i.e., it does not capture pattern emergence *de novo*. Nevertheless, a hierarchy of morphogenetic processes based on positional information, in which an initial morphogen gradient is present in the fertilized egg, and regions established at one level are further patterned at the next level, was found to model segmentation of insect embryos correctly [Lawrence 1992]. The role of morphogen gradients in plant morphogenesis is less well established, but we consider the possibility that they play a role in plant pigmentation.

2.2.3 Reaction-diffusion. Reaction-diffusion, proposed by Turing [1952], was the first model of morphogenesis. Reaction-diffusion systems consist of two or more morphogens that diffuse and react with each other. The equations for an isotropic, deterministic reaction-diffusion system with $n \geq 2$ morphogens $u_1, \ldots, u_n$ have the general form

$$\frac{\partial u_i}{\partial t} = F_i(u_1, \ldots, u_n) + D_i \nabla^2 u_i, \qquad i = 1, \ldots, n, \qquad (1)$$

where functions F_i define the reaction component of the system and scalars D_i are the morphogen diffusivities. Anisotropic diffusion is introduced by replacing the Laplacian with the anisotropic Laplace-Beltrami operator $\nabla \cdot D_i \nabla u_i$, where D_i is the diffusion tensor [Andreux et al. 2015]. Turing discovered that, with appropriately chosen equations, the uniform distribution of morphogens is unstable, and

infinitesimal disturbances lead to the emergence of patterns. Subsequent studies have shown that various types of reactions, including the widely used activator-inhibitor and activator-substrate systems [Gierer and Meinhardt 1972; Meinhardt 1982], exhibit similar behavior. Considering reactions proposed by Gray and Scott [1984], Vastano et al. [1987] demonstrated mathematically, and Pearson [1993] showed with computational models, that patterns may also arise in a different mode, in which the uniform distribution of morphogens is stable. In this case, patterns do not emerge *de novo*, but non-infinitesimal inhomogeneities become elaborated into complex patterns over time. Concurrently with the work of Pearson [1993], Lee et al. [1993] presented experimental evidence of this mode. We considered both the emergent and the inhomogeneity-elaborating modes when constructing our models.

2.2.4 Model integration. Wolpert [1969] introduced positional information as an alternative, rather than complement, to reaction-diffusion. Nevertheless, both concepts have long been used in combination. For instance, Turk [1991] modulated diffusion rates in a reaction-diffusion model of a zebra coat pattern to locally control the width of stripes according to their position on the zebra body. Likewise, Fowler et al. [1992] and Meinhardt [2009] modulated the rate of substrate production to locally control the density of stripes when modeling pigmentation patterns in seashells. Sanderson et al. [2006] presented and analyzed many further examples of the control of reaction-diffusion systems, illustrating them with highly realistic spatially inhomogeneous pigmentation patterns in fish. Green and Sharpe [2015] analyzed the interplay between positional information and reaction-diffusion from a theoretical perspective, distinguishing modes in which positional information controls reaction-diffusion, acts concurrently with it, or arises from it.

In plants, the contributing models may appear in different combinations. For example, the pattern of dots in *Galearis* flowers is limited to parts of the perianth (Fig. 3J), suggesting that reaction-diffusion is controlled by positional information. The pattern of blotches in *Fritillaria* (Fig. 3K) appears to be correlated with the underlying pattern of proximo-distal veins. We designed our modeling system to facilitate modeling such combinations.

2.2.5 Growth. Flower pigmentation is correlated with flower shape, thus a fully emergent model of pigmentation patterning should incorporate flower development. Although methods for simulating flower development have been devised both from the biological [Green et al. 2010; Kennaway et al. 2011] and computer graphics [Owens et al. 2016; Prusinkiewicz et al. 1993] perspectives, the dynamics of petal growth is difficult to measure and is known only in isolated cases [Rolland-Lagan et al. 2003]. Likewise, studies linking the dynamics of flower development to pigmentation patterns [Suzuki et al. 2016] are limited. Consequently, in the scope of this paper we neglect growth, in spite of its impact on patterning shown in other contexts, for example the patterning of sea shells [Fowler et al. 1992; Meinhardt 2009], fish skin [Kondo and Asai 1995] and the skin or fur of other animals [De Gomensoro Malheiros et al. 2020]. Instead, we follow the approach of Turk [1991], who hypothesized that, in some cases, the impact of anisotropic growth on the generated pattern can be approximated using anisotropic diffusion.

2.3 Previous models of flower pigmentation patterns

Within plants, Prusinkiewicz and Lindenmayer [1990] simulated different coloring of ray vs. disk florets in flower heads, and Prusinkiewicz et al. [2001] simulated inflorescences with flower color depending on age. Rodkaew et al. [2002], followed by Runions et al. [2005], proposed generative models of leaf venation, which Runions et al. [2005] applied to model flower venation as well. Zhou et al. [2007] were the first to recognize flower pigmentation patterns as an interesting computer graphics topic on its own. They proposed reaction-diffusion coupled with vasculature as the modeling framework, and suggested using the space colonization algorithm [Runions et al. 2005] to generate the venation patterns. Unfortunately, they illustrated their method with variants of only a single pattern, intermediate between those in Fig. 3, G and H, and did not provide the parameter values needed to reproduce and analyze their results. Such an analysis would be useful, because in our experience similar patterns can be obtained using a single diffusing substance, without involving a full reaction-diffusion system (for example, see the model of *Dianthus* in Section 4.4).

Pursuing other approaches, Lu and Song [2014] realistically modeled pigmentation patterns in *Gazania rigens* heads and *Agrostemma githago* flowers by mapping positions within petals into colors using heuristic functions. While acceptable from an image synthesis perspective, the use of heuristics makes this method less interesting as a means to understand the mechanisms that underlie pigmentation patterns in nature. Risi et al. [2016] generated flowers with pigmentation patterns using a variant of artificial neural networks, and devised an evolutionary technique to diversify their shapes and patterns. The sample flowers have a cartoon-like appearance, consistent with their intended use in a video game, but the evolutionary technique offers an interesting path to model flowers and their pigmentation patterns without intimate knowledge of the underlying equations and parameters.

The work of Zhou et al. [2007] preceded the biological hypotheses postulating reaction-diffusion patterning of flower pigmentation [Albert et al. 2014a; Davies et al. 2012; Yuan et al. 2014]. These hypotheses have recently been confirmed experimentally and illustrated with a computational model of pigmented spots in the flowers of *Mimulus* (monkeyflower) implemented on a square grid [Ding et al. 2020]. Inspired by the same literature, Ringham [2020] proposed several reaction-diffusion models of pigmentation patterns in flowers, including those of *Mimulus*, respecting flower geometry. The work we present here builds upon and extends these results.

3 THE MODELING METHOD
3.1 Overview

We implemented the pipeline shown in Fig. 4 to generate flower pigmentation patterns. The input consists of: (i) a flower shape, specified as a polygon mesh in PLY format; (ii) a prepattern providing additional per-mesh-element information affecting the simulation, such as the initial and boundary conditions; and (iii) equations and parameters for the simulation procedure. The simulation generates a distribution of morphogen concentrations mapped to pigment concentrations using a transfer function (color map) defined by the modeler. The output is another PLY file, with colors representing
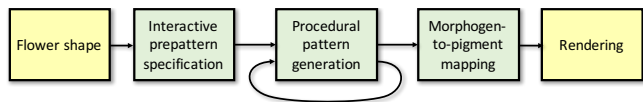
Fig. 4. The modeling pipeline. The stages presented in this paper are shown in green; the stages implemented using existing tools are yellow. The loop indicates that procedural pattern generation (simulation) may consist of a sequence of stages, in which the output of a previous stage becomes the prepattern for the next stage.

pigmentation, which can be rendered directly or incorporated into models of whole plants. Simple patterns are generated in a single pass of the procedure. More complex patterns may require a multi-stage process, such that mesh properties generated in an earlier stage provide the prepattern for the next.

3.2 Flower shape modeling

Many techniques have been proposed to model floral shapes. They include standard geometric modeling techniques using bicubic surfaces [Owens et al. 2016; Prusinkiewicz and Lindenmayer 1990], sketch-based modeling [Ijiri et al. 2005], as well as reconstruction of petal surfaces from point clouds [Zhang et al. 2014] or X-ray computed tomography scans [Ijiri et al. 2014]. In the scope of this paper we found it practical to use the general-purpose mesh editor implemented in Blender [BlenderNation 2021], with modeling guided by reference photographs placed in the background [Flavell 2010]. The interactively defined coarse polygon meshes were smoothed using Catmull-Clark subdivision, then triangulated using the instant field-aligned meshing algorithm [Jakob et al. 2015] implemented in the Instant Meshes software [Jakob 2021]. This algorithm produces meshes with almost equilateral triangles of approximately constant size, which provides good discrete support for the subsequent pattern generation.

3.3 Prepattern specification

In addition to the flower shape, our method requires input that summarizes the effect of processes preceding the simulation. This input defines the initial and boundary conditions for the subsequent simulations, and may include additional spatial information, such as the layout of nectar guides. We refer to this information as a prepattern and specify it either interactively, by painting prepatterns on the meshes representing the flowers [Hanrahan and Haeberli 1990], or by organizing procedural elements of the simulation into a pipeline and considering the output of a previous stage as the prepattern controlling the next stage. The concept of a prepattern is an extension of diffusion maps, introduced by [Witkin and Kass 1991] to locally control anisotropic diffusion. Crucially, they observed that such maps are much coarser — and thus require less input — than the resulting patterns.

3.4 Procedural pattern generation

3.4.1 Vascular pattern modeling. An important aspect of the appearance of many flowers is a conspicuous vein pattern. We model it using the space colonization algorithm introduced by Runions et al. [2005] to model leaf and flower vasculature. The original space colonization algorithm operates in a plane. To extend it to highly curved

flower corollas and calyces, we follow Hädrich et al. [2017], who applied the space colonization algorithm to model plants climbing along arbitrary surfaces. The basic idea is that, at each iteration of the algorithm, vein tips grow towards attraction points — sampled directly from the mesh representing the flower surface — through the ambient space, but then are projected onto the mesh. In this way, the pattern remains on the surface.

3.4.2 Diffusion simulation. Diffusion of morphogens is a fundamental component of models of morphogenesis following both the positional information and reaction-diffusion paradigms. We implemented anisotropic diffusion on a triangle mesh using two methods: (i) based on the equations provided by Andreux et al. [2015], and (ii) derived from first principles by following the rich literature on discrete differential geometry, including [Botsch et al. 2010; Crane et al. 2013; Desbrun et al. 2006; Mancinelli et al. 2019; Meyer et al. 2003]. Both methods produced identical results. Below we present the second method, which is expressed using simpler equations and lends itself directly to a stochastic extension.

According to Fick's law, flux of a diffusing substance is proportional to the gradient of its concentration:

$$\mathbf{J} = -D\nabla c. \tag{2}$$

The diffusion constant D is a scalar in the case of isotropic diffusion, and a tensor in the anisotropic case. Given the field of fluxes, the rate of mass flow into an arbitrary region R of the diffusion domain is

$$\dot{m}(R) = -\oint_{\partial R} \mathbf{J} \cdot \hat{\mathbf{n}} \, dl, \tag{3}$$

where ∂R is the boundary of region R and $\hat{\mathbf{n}}$ is the unit-length normal vector to the boundary element dl, pointing outwards. The average (surface) concentration $c(R)$ of the diffusing substance in region R thus changes at the rate

$$\frac{dc(R)}{dt} = \frac{\dot{m}(R)}{\text{area}(R)}. \tag{4}$$

Equations 2 – 4 constitute a system of ordinary differential equations, which we solve iteratively using the forward Euler method. When setting up these equations for specific models, we assume that the mesh is a Delaunay triangulation of its vertices P. We then associate concentrations $c(P)$ with these vertices, gradients ∇c and fluxes $\mathbf{J}$ with the triangles, and regions $R(P)$ between which the substance flows as the Voronoi polygons surrounding each vertex P (e.g., vertex B in Fig. 5A). Assuming that the initial concentrations $c(P)$ are given, in a single simulation step we then calculate: (i) the concentration gradient ∇c within each triangle T of the mesh; (ii) the resulting fluxes $\mathbf{J}$; (iii) the rate of mass flow $\dot{m}(P)$ into Voronoi polygon $R(P)$ surrounding vertex P; and (iv) the resulting change in average concentration $c(P)$.

Gradient calculation. To calculate the gradient, we approximate the field of concentrations within each triangle as a linear combination of the concentrations at the vertices (Fig. 5B). Given a triangle ABC, we calculate the contribution of a vertex, say B, to the gradient, by setting the concentrations of the remaining vertices to zero. The
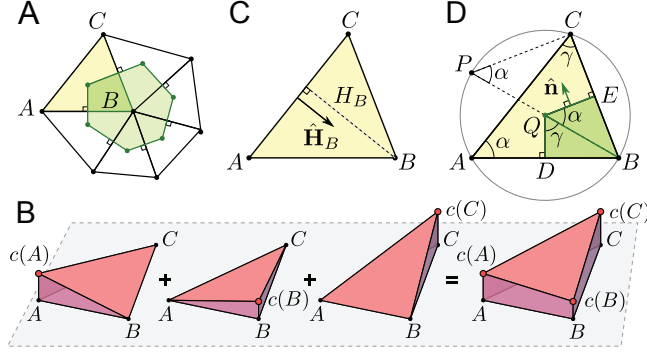
Fig. 5. Elements of the diffusion simulation. (A) Discretization of the manifold in proximity of sample vertex B: Delaunay triangles sharing vertex B (white and yellow), and Voronoi polygon $R(B)$ surrounding vertex B (green). Derivation of the equations is focused on triangle ABC and the part of the Voronoi polygon that $\triangle ABC$ intersects. (B) Gradient ∇c in triangle ABC is approximated by the sum of the linear gradients contributed by all vertices. (C,D) Symbols used in equations.

contribution of concentration $c(B)$ thus is

$$\frac{c(B)}{H_B}\hat{\mathbf{H}}_B, \tag{5}$$

where H_B is the length of the vector $\mathbf{H}_B$ that is perpendicular to edge AC and points to vertex B, and $\hat{\mathbf{H}}_B$ is the unit vector in the direction of $\mathbf{H}_B$ (Fig. 5C). As the gradient operator is linear, the gradient of concentration ∇c in triangle ABC is the sum of the gradients contributed by all vertices:

$$\nabla c(\triangle ABC) = \frac{c(A)}{H_A}\hat{\mathbf{H}}_A + \frac{c(B)}{H_B}\hat{\mathbf{H}}_B + \frac{c(C)}{H_C}\hat{\mathbf{H}}_C. \tag{6}$$

Let $\mathbf{N}$ denote a vector perpendicular to triangle ABC such that $N = 2\cdot\text{area}(\triangle ABC)$ (for example, $\mathbf{N}$ can be calculated as the cross product $\vec{AB}\times\vec{BC}$). We then observe that $||\vec{CA}||H_B = 2\cdot\text{area}(\triangle ABC) = N$, which implies that $1/H_B = ||\vec{CA}||/N$ and

$$\frac{\hat{\mathbf{H}}_B}{H_B} = \frac{||\vec{CA}||\hat{\mathbf{H}}_B}{N} = \frac{\vec{CA}^\perp}{N} = -\frac{\vec{CA}\times\hat{\mathbf{N}}}{N} = -\frac{\vec{CA}\times\mathbf{N}}{NN} = -\frac{\vec{CA}\times\mathbf{N}}{\mathbf{N}\cdot\mathbf{N}}.$$

Here $\vec{CA}^\perp$ denotes the vector obtained by rotating $\vec{CA}$ by $90°$ with respect to $\mathbf{N}$. Similar equalities hold for $\frac{\hat{\mathbf{H}}_A}{H_A}$ and $\frac{\hat{\mathbf{H}}_C}{H_C}$. By substituting them into Equation 6 and factoring out the common term we obtain:

$$\nabla c(\triangle ABC) = -\left(c(A)\vec{BC} + c(B)\vec{CA} + c(C)\vec{AB}\right)\times\frac{\mathbf{N}}{\mathbf{N}\cdot\mathbf{N}}. \tag{7}$$
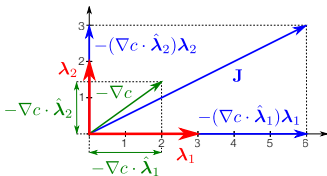
Flux calculation. In the isotropic case, we calculate flux directly from Equation 2. In the anisotropic case, we assume that diffusion tensor D is defined by a pair of orthogonal (eigen)vectors λ_1 and λ_2, which specify diffusion rates in their respective directions [Wilson and Gibbs 1901]. We then decompose gradient ∇c in these directions, calculate flux in each direction using

vector length $||\lambda_1||$ or $||\lambda_2||$ as the diffusion constant, and add the results:

$$\mathbf{J} = -\left(\nabla c\cdot\hat{\lambda}_1\right)\lambda_1 - \left(\nabla c\cdot\hat{\lambda}_2\right)\lambda_2. \tag{8}$$

Mass flow calculation. We now calculate the rates of mass flow into the Voronoi polygons associated with each vertex of the mesh. Consider polygon $R(B)$ surrounding vertex B and mass flow through its edge EQ (Fig. 5D). From triangle BEQ we find that $||\vec{EQ}|| = ||\vec{BE}||\cot\alpha$. According to the definition of Voronoi diagrams

$$||\vec{BE}|| = \frac{1}{2}||\vec{BC}||, \tag{9}$$

and vector $\vec{EQ}$ is perpendicular to vector $\vec{BC}$; consequently

$$\vec{EQ} = \frac{1}{2}\vec{BC}^\perp\cot\alpha. \tag{10}$$

Following Equation 3, the contribution of the mass flow through edge EQ to the total flow into polygon $R(B)$ is thus

$$\dot{m}_{EQ} = \mathbf{J}\cdot\hat{\mathbf{n}}\,||\vec{EQ}|| = \mathbf{J}\cdot\vec{EQ}^\perp = \mathbf{J}\cdot\left(\frac{1}{2}\vec{BC}^\perp\right)^\perp\cot\alpha = -\frac{1}{2}\mathbf{J}\cdot\vec{BC}\cot\alpha.$$

According to elementary geometry, $\alpha = \angle EQB = \frac{1}{2}\angle CQB = \angle CAB$. The value $\cot\alpha$ can thus be calculated as

$$\cot\alpha = \frac{\cos\alpha}{\sin\alpha} = \frac{\hat{AB}\cdot\hat{AC}}{||\hat{AB}\times\hat{AC}||} = \frac{\vec{AB}\cdot\vec{AC}}{||\vec{AB}\times\vec{AC}||}. \tag{11}$$

The rate of mass flow through edge DQ can be calculated in the same way. Taking into account that vector $\vec{DQ}$ within triangle QDB is oriented opposite to vector $\vec{EQ}$ within triangle BEQ, the total rate of mass flow from triangle ABC into the Voronoi polygon $R(B)$ is

$$\dot{m}(\triangle ABC \to R(B)) = \frac{1}{2}\mathbf{J}\cdot\left(-\vec{BC}\cot\alpha + \vec{AB}\cot\gamma\right). \tag{12}$$

By performing similar calculations for all Delaunay triangles sharing vertex B and summing the results, we obtain $\dot{m}(R(B))$, the total rate of mass flow into the Voronoi polygon surrounding vertex B.

Calculation of concentration changes. To estimate how mass flow affects concentrations, we calculate the areas of Voronoi polygons surrounding all vertices of the mesh. Focusing on vertex B (Fig. 5D), and taking into account Equations 9 and 10, triangle BEQ contributes towards polygon $R(B)$ the area:

$$\frac{1}{2}||\vec{BE}||\,||\vec{EQ}|| = \frac{1}{2}\left(\frac{1}{2}||\vec{BC}||\right)\left(\frac{1}{2}||\vec{BC}||\cot\alpha\right) = \frac{1}{8}\vec{BC}\cdot\vec{BC}\cot\alpha.$$

With a similar formula for the contribution of triangle BQD, the total contribution of triangle ABC towards the area of Voronoi polygon $R(B)$ is

$$\text{area}(\triangle ABC \to R(B)) = \frac{1}{8}\left(\vec{BC}\cdot\vec{BC}\cot\alpha + \vec{AB}\cdot\vec{AB}\cot\gamma\right). \tag{13}$$

As in the case of fluxes, the total area of Voronoi polygon $R(B)$ is calculated by adding the contributions of all mesh triangles sharing vertex B. The rate of concentration change at each vertex is then obtained by dividing the rate of mass flow into the Voronoi polygon associated with the vertex by the polygon area (Eq. 4).

Randomization. We now take into account the stochastic character of diffusion. Consider edge EQ of the Voronoi polygon surrounding vertex B (Fig. 5D). As all operations involved in the calculation of

fluxes are linear, the rate $\dot{m}_{EQ}$ of mass flow through edge EQ can be decomposed into three rates, $\dot{m}_{EQ}(A)$, $\dot{m}_{EQ}(B)$ and $\dot{m}_{EQ}(C)$, such that each rate is the product of the diffusing substance concentration at the respective vertex and a constant that depends only on the geometry of triangle ABC and the diffusion tensor (λ_1, λ_2). For example,

$$\dot{m}_{EQ}(C) = c(C)Z_C, \qquad (14)$$

where

$$Z_C = \frac{1}{2}(((\vec{AB} \times \frac{\mathbf{N}}{\mathbf{N} \cdot \mathbf{N}}) \cdot \hat{\lambda}_1)\lambda_1 + ((\vec{AB} \times \frac{\mathbf{N}}{\mathbf{N} \cdot \mathbf{N}}) \cdot \hat{\lambda}_2)\lambda_2) \cdot \vec{BC} \cot \alpha.$$

Let Ω be the coefficient of proportionality that converts masses into molecule numbers. We then rewrite Equation 14 as

$$\Omega \dot{m}_{EQ}(C) \Delta t = \underbrace{\Omega c(C) \, \mathrm{area}(R(C))}_{\eta} \underbrace{(Z_C / \mathrm{area}(R(C)))}_{k} \Delta t, \qquad (15)$$

where Δt is the time increment over which mass flow takes place, and $\mathrm{area}(R(C))$ is the area of the Voronoi polygon surrounding vertex C. Equation 15 has the form of an update formula for the number of molecules η in a monomolecular reaction occurring with reaction rate k over time increment Δt. Taking into account the stochastic character of individual reactions at the molecular level, their macroscopic outcome can be approximated as the Chemical Langevin Equation [Gillespie 2000, 2007]:

$$\Omega \dot{M}_{EQ}(C) \Delta t = \eta k \Delta t + \sqrt{\eta |k| \Delta t} \, \mathcal{N}(0,1), \qquad (16)$$

or

$$\dot{M}_{EQ}(C) \Delta t = c(C) Z_C \Delta t + \sqrt{\frac{1}{\Omega} c(C) |Z_C| \Delta t} \, \mathcal{N}(0,1). \qquad (17)$$

Here $\dot{M}_{EQ}(C)$ is the random variable representing the average reaction rate over time interval Δt, and $\mathcal{N}(0,1)$ is the normally distributed random number with mean zero and standard deviation one. By using analogous estimates for all components of mass flow across Voronoi polygon edges in the mesh, we obtained the final algorithm for the stochastic simulation of anisotropic diffusion in a triangle mesh, where parameter Ω controls randomness in a manner independent of the size of triangles and time step Δt.

3.4.3 Reaction-diffusion. We employed several variants of reaction-diffusion systems. The equations are given in the context of specific models (Section 4). Like diffusion, reactions can be simulated using stochastic methods, including the Chemical Langevin Equation [Gillespie 2000, 2007], but we have only employed deterministic reactions in the presented models.

3.4.4 Random point generation. The need to select mesh vertices randomly occurs in two contexts. First, the vertices may approximate positions of pigmentation speckles in patterns that result from the random excision of transposable elements (transposons) from the genome of individual cells (Fig. 3L). Second, they may represent inhomogeneities in morphogen distributions acted upon by the subsequent patterning processes. To generate points with approximately uniform distribution, we enumerated all N vertices in the mesh, then selected the desired number of sample points using a random number generator producing uniformly distributed integer numbers in the interval $[1, N]$. The resulting points were distributed almost uniformly on the supporting surface due to the

approximately constant density of vertices resulting from the Instant Meshes algorithm. To generate patterns with a given probability density function $f : P \rightarrow [0, 1]$ of position P, we applied the sample rejection method [Ross 1997], which consists of: (i) choosing a candidate sample point P (from a uniform distribution), as described above; (ii) generating a uniformly distributed random number $p \in [0, 1]$; (iii) accepting point P if $p < f(P)$ or rejecting it otherwise; and (iv) iterating the above process until the desired number of points has been selected.

3.4.5 Model integration. In multistage models, patterns generated in earlier stages may control boundary conditions, initial values or parameters of generative procedures operating in the next stage (Fig. 4). Control of scalar values by a prepattern is conceptually straightforward. Slightly more complex is the use of a prepattern to orient vectors λ_1 and λ_2, which define anisotropic diffusion at the next stage. To this end, we first simulate the diffusion of a control (prepattern) morphogen G between predefined sources and sinks, and calculate its concentration gradient ∇g. We then define vectors λ_1 and λ_2 as

$$\lambda_1 = \lambda_1 \hat{\nabla} g, \quad \text{and} \quad \lambda_2 = \lambda_2 (\hat{\nabla} g)^{\perp}. \qquad (18)$$

As the normalized vector $\hat{\nabla} g$ is defined only when $\nabla g \neq 0$, we calculate flux $\mathbf{J}$ using Equations 8 and 18 in the anisotropic case, and using Equation 2 in the isotropic case.

3.5 Morphogen-to-pigment mapping and rendering

We mapped morphogen concentrations to colors phenomenologically, by applying user-defined color maps to match colors observed in nature. To render flowers realistically we used the LuxCore physically-based renderer integrated into Blender. Material settings were inspired by an analysis of the optical properties of flowers [van der Kooi et al. 2016], including the relative proportions of color-selective absorption, reflectance and transmission, and the importance of light backscattering within the inner petal tissue (mesophyll). When appropriate, we have added geometric details such as hairs in the rendering process, to improve the visual presentation of the plants.

4 CASE STUDIES

We investigated the potential of the above processes to generate flower pigmentation patterns in a series of case studies, guided by the classification of patterns in Section 2.1. Additional data regarding the models are provided in Table 1 (Section 5).

4.1 Platycodon grandiflorus

Veins are a feature in the appearance of many flowers, and in some cases proximity to veins is the main factor driving pigmentation [Schwinn et al. 2006]. An example is the *Platycodon grandiflorus* (blue balloon) flower. The intricate vascular pattern generated on the petal surface is shown in Fig. 6, and the rendered model is compared with a *Platycodon* photograph in Fig. 7.

4.2 Arctostaphylos uva-ursi

Pigmentation of *Arctostaphylos uva-ursi* (bearberry) flowers transitions smoothly between the white tube and pink lobes, providing
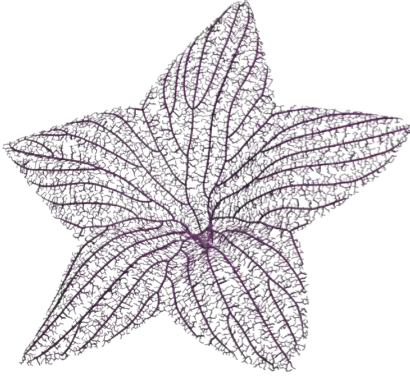
Fig. 6. The intricate pattern of veins generated on the partially fused corolla of *Platycodon grandiflorus*.

Fig. 7. Model and photograph of a *Platycodon grandiflorus* flower.

a simple example of non-uniform coloring associated with position (Fig. 8). We modeled this pattern by simulating the diffusion of a pink-inducing morphogen from the lobe margins toward the pedicel, stopping the simulation when the morphogen reached approximately $\frac{1}{3}$ of the distance toward the pedicel. The diffusion had a stochastic component, which captured small irregularities of coloring, most visible where the red pigment is almost disappearing. The patterning of sepals was simulated in a similar way, with the colors reversed (white boundary, pink centers).

Fig. 8. Model and photograph of *Arctostaphylos uva-ursi* flowers. Model parameters: $D = 1$, $\Omega = 10^{-7}$, $\Delta t = 10^{-5}$.

4.3 Primula x polyantha

Primula x *polyantha* Gold Lace Black flowers have five petals, with dark spots located symmetrically in the two lobes of each petal. The well-defined location of these spots suggests another pattern controlled by positional information. We modeled it by assuming diffusion of a morphogen from the sources — short radial lines near the center of each lobe (Fig. 9A) — towards the sink at the petal boundary. In contrast to the bearberry model, we employed a step transfer function mapping morphogen values to pigment colors. Deterministic diffusion yields regular spots with smooth edges (Fig. 9B), whereas noise inherent in stochastic diffusion introduces irregularities at the spot boundaries (Fig. 9, C and D). A properly selected noise level approximates patterns observed in the reference plant (Fig. 10).
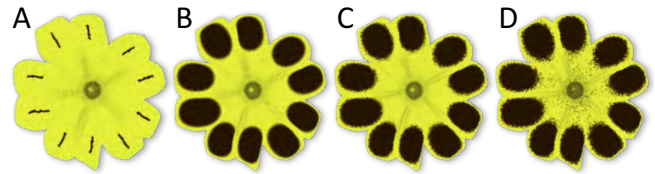

Fig. 9. The impact of noise on the appearance of pigmented spots modeled using stochastic diffusion with increasing randomness. (A) The interactively specified (painted) prepattern. (B) Pigmented spots modeled using deterministic diffusion with $D = 10^{-3}$, $\Delta t = 10^{-3}$. (C, D) Pigmented spots modeled using stochastic diffusion with $\Omega = 10^7$ and $\Omega = 2.5 \cdot 10^6$, respectively.

Fig. 10. Model and photograph of a *Primula* x *polyantha* Gold Lace Black flower. Model parameters as in Fig. 9C.

4.4 Dianthus barbatus

Dianthus barbatus is a popular ornamental plant with radially symmetric flowers, each producing five petals. The proximal and distal zones of each petal are white, whereas the central zone is red. From a modeling perspective, the challenging feature of this pattern is the irregularity of the zone boundaries. It is significantly larger than that of the *Primula* spots (Fig. 10) and cannot be reproduced simply by increasing the random term in the stochastic diffusion equation (Eq. 17). Hypothesizing that vasculature plays a role, we have modeled this pattern by assuming a single morphogen that diffuses faster along the veins than outside of them (Fig. 11). The morphogen source was a curved band running across each petal.
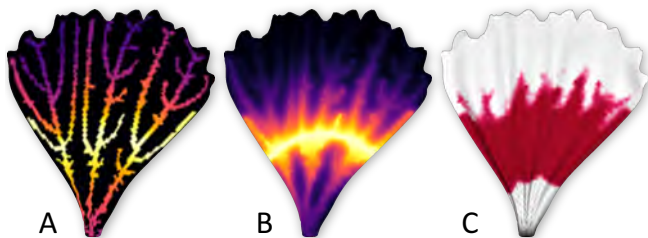
Fig. 11. Construction of the *Dianthus* petal pigmentation model. (A) Concentrations of a morphogen diffusing along the veins from sources located approximately $\frac{1}{3}$ of distance from the petal base to its margin. (B) Extension of model (A), with the morphogen assumed to also diffuse from the veins to the surrounding tissue. (C) Final pigmentation model, resulting from a non-linear mapping of morphogen concentrations (B) to pigment colors. Model parameters: $D = 3$ (veins), $7.5 \cdot 10^{-3}$ (elsewhere), $\Omega = 10^6$, $\Delta t = 10^{-4}$.

Fig. 12. Model and photograph of a *Dianthus barbatus* flower.

The simulation was stopped before the morphogen reached the petal margins. An irregular pattern emerged, approximating that of the real flower (Fig. 12).

4.5 Mimulus guttatus

Mimulus (monkeyflower) is a genus of wildflowers exhibiting diverse pigmentation patterns [Yuan 2019]. Among them, *M. guttatus* was one of the first plant species for which the flower patterning was analyzed down to the molecular level [Ding et al. 2020; Yuan et al. 2014]. The key molecular players are the proteins NEGAN and RTO, which interact with the kinetics of an activator-inhibitor system. Ding et al. [2020] simulated an essential feature of this pattern — dispersed dots — using the system of equations introduced by Gierer and Meinhardt [1972]; Meinhardt [1982]:

$$\begin{aligned}
\frac{\partial a}{\partial t} &= \rho_a \frac{a^2}{h + \kappa} + \rho_{a0} - \mu_a a + D_a \nabla^2 a, \\
\frac{\partial h}{\partial t} &= \rho_h a^2 + \rho_{h0} - \mu_h h + D_h \nabla^2 h.
\end{aligned} \tag{19}$$

Here a represents the concentration of NEGAN, the activator, and h is the concentration of RTO, the inhibitor. The model of Ding et al. [2020], however, was implemented on a square grid and did not capture a distinctive feature of the *M. guttatus* pattern: its correlation with the flower shape. To incorporate this feature, we define a prepattern that constrains base production of NEGAN, ρ_{a0}, to select
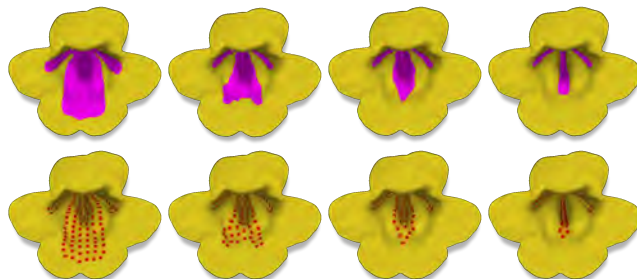

Fig. 13. Relation between painted prepatterns (top) and the resulting *Mimulus guttatus* pigmentation patterns (bottom) generated by the activator-inhibitor model (Eq. 19) with parameters: $\rho_a = 0.05$, $\rho_{a0} = \{0, 0.0125\}$, $\kappa = 0$, $\mu_a = 0.05$, $\rho_h = 0.05$, $\rho_{h0} = 0$, $\mu_h = 0.08$, $D_a = 2.5 \cdot 10^{-5}$, $D_h = 0.001$, $\Delta t = 0.06$.

regions of the plant corolla (Fig. 13, top). Dots are then generated only where specified by the prepattern (Fig. 13, bottom). With a properly chosen prepattern, the simulated pattern closely resembles that observed in nature (Fig. 1).

4.6 Digitalis purpurea

The flowers of *Digitalis purpurea* (foxglove) have a scattered pattern of dark purple spots on the bottom side of the tubular corolla. These spots are surrounded by white halos, which can merge with the halos around nearby spots. The remainder of the corolla is pink or light purple. We have modeled this pattern by employing the same activator-inhibitor system as for *Mimulus* (Eq. 19). To capture the unequal distribution of spots, we initiated reaction-diffusion with 83 seed points of high activator concentration, located primarily at the bottom of the corolla tube (Fig. 14). These points were selected using the rejection method (Section 3.4.4), with density controlled by an intermediate morphogen G. The concentrations of G were determined, in turn, through diffusion between interactively specified lines with minimum and maximum concentration. Various configurations of seed points resulted in patterns that are similar, yet different in details, reflecting the natural diversity of foxglove flowers (Fig. 15).

Initially, the activator is present only at the seed points. As the simulation progresses, activator concentrations increase everywhere due to local production. The halos arise as the inhibitor, the production of which is promoted by the activator, diffuses away from the high-concentration spots, reducing the production of the activator around them. At this stage, reaction-diffusion elaborates the initial pattern of seed points, rather than generating a pattern *de novo*. In the steady state, though, the pattern would stabilize with spots distributed uniformly throughout the entire corolla. The foxglove flower pigmentation model thus reflects a transient, rather than steady-state, distribution of the activator.

4.7 Kohleria

Kohleria is a genus of tropical plants popular as house plants. Many species and hybrids have intricate pigmentation patterns, which makes them challenging from a modeling perspective. The flowers we chose to model are red on the abaxial side and white with a red pattern on the adaxial side. The pattern consists of a network
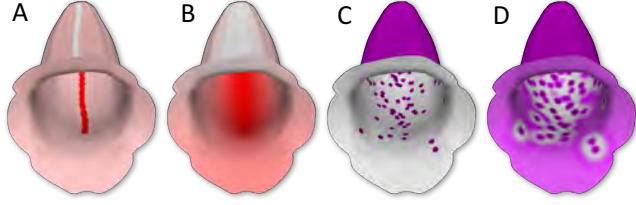
Fig. 14. Modeling *Digitalis purpurea* (common foxglove) flower pigmentation. (A) The painted prepattern. (B) Establishment of positional information by an intermediate morphogen diffusing in the corolla, with the boundary conditions partially specified by the prepattern. (C) Generation of seed points with density controlled by the intermediate morphogen G. (D) The resulting pattern simulated using the activator-inhibitor model (Eq. 19) with parameters: $\rho_a = 0.05$, $\rho_{a0} = 0.0125$, $\kappa = 0.001$, $\mu_a = 0.05$, $\rho_h = 0.05$, $\rho_{h0} = 0$, $\mu_h = 0.08$, $D_a = 4.0 \cdot 10^{-5}$, $D_h = 1.5 \cdot 10^{-3}$, $\Delta t = 0.005$.

Fig. 15. Model and photograph of a foxglove inflorescence. Photograph by Wolfgang Claussen, adapted under the Pixabay licence.

of branching and interconnected lines, radiating from the flower center (throat), which transitions to a pattern of dots toward the petal margins. We modeled this pattern using one of the reaction-diffusion systems proposed by Turing [1952], extended to allow for anisotropic diffusion of morphogen U:

$$
\begin{aligned}
\frac{\partial u}{\partial t} &= \rho(\alpha - uv) + D_u \nabla^2 u, \\
\frac{\partial v}{\partial t} &= \rho(uv - v - \beta) + \nabla \cdot D_v \nabla v.
\end{aligned}
\tag{20}
$$

The pattern is locally controlled by morphogen G which diffuses isotropically from the petal margins, where its concentration is set to 1, to the flower throat, where its concentration is set to 0 (Fig. 16 A-C). The positional information established by concentrations g of morphogen G plays two roles. First, it controls local production of morphogen U via the nonlinear function

$$
\alpha = \alpha_{min} + (\alpha_{max} - a_{min})g^\gamma,
\tag{21}
$$

where α_{min}, α_{max} and γ are predefined parameters. Second, it controls diffusion of morphogen V: the gradient ∇g determines the directions of vectors $\boldsymbol{\lambda}_{v1}$ and $\boldsymbol{\lambda}_{v2}$ that define the diffusion tensor D_v (Eq. 18), whereas the concentration g controls the magnitude of diffusivity (vector length) λ_{v2}. With $\alpha = \alpha_{max}$, diffusion is isotropic and Equations 20 produce spots characteristic of the outer petal zone. Decreasing α to α_{min} changes this pattern to a network of lines
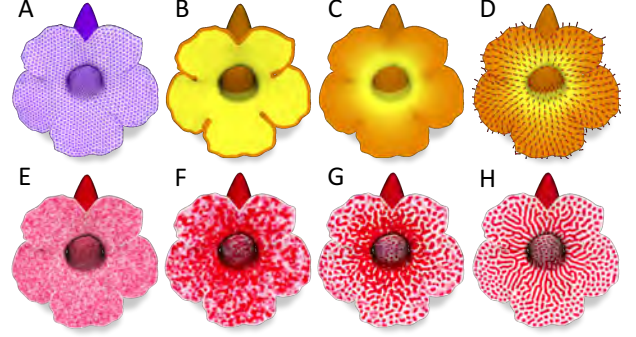
Fig. 16. Modeling *Kohleria* flower pigmentation. (A) The triangle mesh representing flower shape. (B) The painted prepattern. (C) Positional information field established by morphogen G diffusing in the corolla with the boundary values given by the prepattern. (D) Gradient of G concentrations. (E–H) Pattern development simulated using Turing's reaction-diffusion model (Eq. 20) with parameters: $\rho = 0.035$, $\alpha = [13.5, 16.25]$, $\beta = 12$, $D_u = 0.18$, $\lambda_{v1} = 0.0375$, $\lambda_{v2} = [0.0135, 0.0375]$, $\gamma = 10$, $\Delta t = 0.2$.

Fig. 17. Model and photograph of a *Kohleria* flower. Photograph by Jane Williams reproduced under fair use / orphan work policies.

running predominantly in the proximo-distal direction due to the anisotropy of the diffusion of v, as observed near the flower center. Fig. 16 E–H illustrates the development of the *Kohleria* pigmentation pattern over time, and Fig. 17 compares the resulting flower model to the photograph of a reference flower.

4.8 Trichoglottis smithii

Flowers of the orchid *Trichoglottis smithii* have a remarkable pattern of irregular, interspersed orange and yellow stripes running across the tepals. We have generated this pattern using the Turing reaction-diffusion model described by Eq. 20, extended to allow for anisotropic diffusion of both morphogens. To orient the pattern across the tepals, we assumed that both morphogens, U and V, diffuse more slowly in the proximo-distal direction than in the medio-lateral direction. To capture the clearly observable increase of the pattern scale away from the flower center, we decreased the value of parameter ρ from 0.005 near the center to 0.001 at the tepal
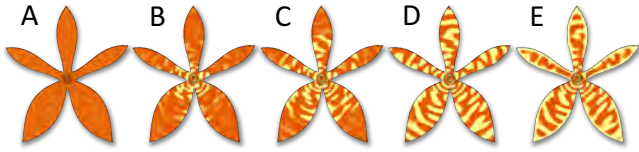
Fig. 18. Development of a simulated *Trichoglottis* tepal pigmentation pattern. Progression (A) to (D) represents the 60,000 steps in Phase 1; image (E) resulted from an additional 4,500 steps in Phase 2. Pattern simulated using Turing's reaction-diffusion model (Eq. 20) with parameters: $\rho = [0.001, 0.005]$, $\alpha = 16$, $\beta = 12$, $\lambda_{u1} = 0.0049$, $\lambda_{u2} = 0.4$, $\lambda_{v1} = 0.001225$, $\lambda_{v2} = 0.01$, $\Delta t = 0.05$.

Fig. 19. Model and photograph of a *Trichoglottis* flower. The background in the photograph was modified using Photoshop to better expose the flower.
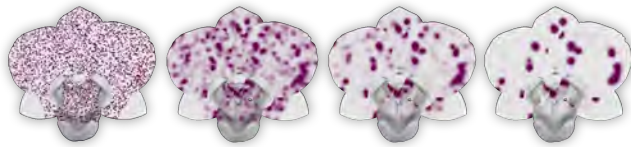

Fig. 20. Spot coalescence during a simulation of *Phalaenopsis* Nankung's 4.55PM tepal pigmentation using the activator-substrate model (Eq. 22) operating in the Gray-Scott regime. Model parameters: $\rho = 1$, $\rho_{a0} = 0$, $\mu_a = 0.145$, $\rho_{s0} = 0.082$, $\mu_s = 0.082$, $D_a = 0.25$, $D_s = 0.5$, $\Delta t = 0.3$.

tips. The simulation proceeded in two phases. In Phase 1 (60,000 steps), we assumed no-flux boundary conditions for both U and V. The resulting pattern (Fig. 18D) resembled that observed in the reference plant (Fig. 19, right), except that the orange stripes, representing areas of low V concentrations, extended to the tepal edges. In contrast, the reference plant had non-pigmented (yellow) borders. To capture this detail, we introduced a second simulation phase, in which we changed the boundary conditions along distal parts of the margin from no-flux to Dirichlet conditions, with $u = 0$ and $v = 30$. A yellow pattern boundary resulted, with the width controlled by the number of simulation steps. The results shown in Fig. 18E and Fig. 19, left, were obtained after 4,500 Phase-2 steps.

4.9 Phalaenopsis Nankung's 4.55PM

The irregular, non-uniformly distributed pigmentation spots characteristic of the *Phalaenopsis* Nankung's 4.55PM orchid cultivar do not

Fig. 21. Model and photograph of a *Phalaenopsis* Nankung's 4.55PM flower.

belong to the spectrum of patterns known to spontaneously emerge from reaction-diffusion. They are visually related, however, to the pattern of lesions occurring in the skin disease psoriasis, which has been reproduced using a Gray-Scott model that elaborated a random pattern of initial perturbations [Ringham et al. 2019]. Consequently, we have modeled the patterning of *Phalaenopsis* Nankung's 4.55PM tepals in a similar manner.

We describe our model in terms of the activator-substrate model [Gierer and Meinhardt 1972; Meinhardt 1982]:

$$\begin{aligned}\frac{\partial a}{\partial t} &= \rho s a^2 + \rho_{a0} - \mu_a a + D_a \nabla^2 a, \\ \frac{\partial s}{\partial t} &= -\rho s a^2 + \rho_{s0} - \mu_s s + D_s \nabla^2 s,\end{aligned} \tag{22}$$

which is equivalent, up to parameter substitution, to the Gray-Scott model [Yamamoto et al. 2011]. The initial pattern consisted of 5,000 random seed points, with the activator concentration a at each point selected, also at random, from the interval $[0, 1]$. The remaining mesh points had an initial activator concentration $a = 0$, and all points have the same initial substrate concentration $s = 1$. With properly chosen parameter values, closely positioned pigmentation points coalesced and grew into larger pigmented regions, whereas more isolated points disappeared (Fig. 20). As for other models, the general character of the pattern does not depend on the distribution of the seed points, although details vary. An alternative pattern and a reference photograph are shown in Fig. 21.

4.10 Phalaenopsis Chian Xen Leopard Stripes

The orchid cultivar *Phalaenopsis* Chian Xen Leopard Stripes is representative of flowers in which the pigmentation pattern is related to vasculature. We simulated this pattern — radially spreading, branching strings of dots — with the activator-inhibitor model (Eq. 19) controlled by two prepatterns. The first prepattern is the vasculature (Fig. 22A), which increases the production of the activator (parameter ρ_{a0}) in proximity to the veins. The second prepattern provides positional information and is defined by a morphogen diffusing away from the flower center. Its concentrations control the diffusion rates of both the activator and the inhibitor, with the effect of reducing the size of pigmented dots toward the flower boundary (Fig. 22B). The range of changes depends on the organ type, differentiating the patterns of dots in the left and right petals from those in the sepals, and imposing solid colors on the flower lip and column.
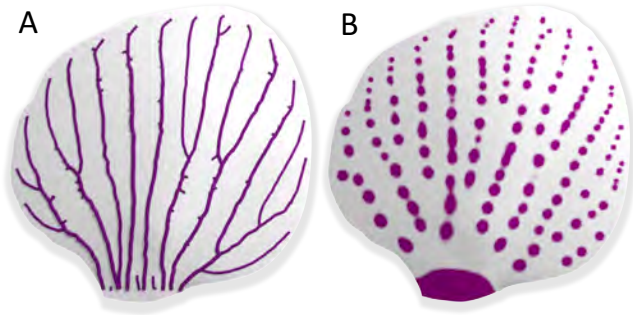
Fig. 22. Key elements of the *Phalaenopsis* Chian Xen Leopard Stripes flower pigmentation model. (A) A vascular pattern generated on a petal by the space colonization algorithm. (B) The pigmentation pattern generated by the activator-inhibitor model (Eq. 19) controlled by the vascular pattern and positional information. Model parameters: $\rho_a = 0.08$, $\rho_{a0} = [6.5 \cdot 10^{-5}, 0.011]$, $k = 0.001$, $\mu_a = 0.03$, $\rho_h = 0.12$, $\rho_{h0} = 0$, $\mu_h = 0.03$, $D_a = [9.56 \cdot 10^{-6}, 3.92 \cdot 10^{-5}]$, $D_h = [4.78 \cdot 10^{-4}, 1.96 \cdot 10^{-3}]$, $\Delta t = 0.05$.

Fig. 23. Model and photograph of a *Phalaenopsis* Chian Xen Leopard Stripes flower. Petal model parameters as in Fig. 22; sepal parameters: $\rho_a = 0.08$, $\rho_{a0} = [1.3 \cdot 10^{-4}, 0.022]$ (left/right), $[1.3 \cdot 10^{-6}, 2.2 \cdot 10^{-4}]$ (top), $k = 0.001$, $\mu_a = 0.03$, $\rho_h = 0.12$, $\rho_{h0} = 0$, $\mu_h = 0.03$, $D_a = 7.13 \cdot 10^{-6}$, $D_h = 3.56 \cdot 10^{-4}$.

5 SOFTWARE IMPLEMENTATION AND PERFORMANCE

To obtain the reported results, we implemented our method as a program called rdpg (**r**eaction-**d**iffusion **p**attern **g**enerator). Rdpg was written in C++ using the OpenGL 4.6 graphics and the Dear ImGui 1.8 user interface libraries. The main object on which it operates is a half-edge data structure representing a triangulated flower shape. Per-element properties, such as vertex positions, indices of adjacent elements, and morphogen concentrations, are stored as OpenGL Shader Storage Buffer Objects (SSBOs). The rdpg simulations can be executed on a CPU or on a GPU supporting OpenGL 4.6.

Model development is facilitated by allowing interactive specification and modification of equations without restarting the program. Inspired by shading languages [Cook 1984], procedural textures [Perlin 1985], and L-systems [Prusinkiewicz and Lindenmayer 1990], we specify these equations as simple scripts. For example, after defining constants a_min, a_max, gamma, rho, and beta, Equations 20 and 21 underlying the *Kohleria* model are specified as follows:

```
Prepattern p;
Morphogens u, v;
```

```
float alpha = lerp(a_min, a_max, pow(p, gamma));
u' = rho*(alpha-u*v) + diffusion(u);
v' = rho*(u*v-v-beta) + diffusion(v);
```

When simulating models using the CPU, this script is translated into a snippet of C++ code, which is compiled and dynamically linked with the executable rdpg code. Alternatively, when using the GPU, it is compiled into a compute shader at runtime. This use of a script required solving two technical problems. One is the partition of computation into the generic component, carried out by rdpg (iteration over mesh elements and calculation of diffusion), and the model-specific component, executed by the code specified by the script (reactions). The second problem is the communication between these components, allowing for the use of variable names that were not known to rdpg at the time of its compilation within the script. Similar problems were recognized and solved in the design and implementation of the L-system-based modeling language L+C [Karwowski and Prusinkiewicz 2003]. We adopted the techniques proposed there to implement scripting in rdpg.

The times needed to generate the patterns described in the present paper are collected in Table 1. As expected, the multi-threaded CPU mode was approximately an order of magnitude faster than single-threaded mode. The GPU mode was approximately as fast as the multi-threaded CPU mode. Better performance can likely be achieved by replacing our simple SSBO-based implementation with a GPU-optimized implementation of reaction-diffusion on a mesh [Descombes et al. 2015]. Nevertheless, the speed of rdpg was adequate for interactive experimentation with equations and parameters during model development.

Name	Fig.	Trian-gles	Steps	CPU 1 thread (m:s)	CPU 16 threads (m:s)	GPU (m:s)
Arcto. (1 flower)	8	53,626	1,500	00:50	0:07	0:01
Primula	10	40,023	2,000	00:37	0:05	0:01
Dianthus (1 petal)	12	9,163	20,000	01:10	0:11	0:07
Mimulus	1	175,968	17,500	23:44	3:11	2:04
Digitalis (1 flower)	15	27,814	19,000	01:22	0:11	0:23
Kohleria	17	98,250	5,697	04:14	0:30	0:19
Trichoglottis	19	21,147	64,500	02:21	0:26	0:33
Phalaenopsis N.	21	64,191	175	00:03	0:01	0:01
Phalaenopsis C.	23	168,394	6,900	10:10	1:09	0.48

Table 1. Timing of final patterning (diffusion or reaction-diffusion) for the implemented models. All simulations were carried out using the AMD Ryzen 7 5800X 3.80GHz 8-core CPU and NVIDIA GeForce RTX 2070 SUPER GPU, running under the Windows 10 operating system.

6 DISCUSSION AND OPEN PROBLEMS

To date, biologists have analyzed the patterning of flowers in only a few plant species. It is known, however, that the molecular-level mechanisms involved in patterning are highly conserved across distant plant families [Albert et al. 2014b; Ding et al. 2020]. Moreover, closely related plants, including varieties of the same species, often exhibit strikingly different patterns. It is thus likely that the diversity of flower pigmentation patterns results from modifications and combinations of common mechanisms, rather than the operation of qualitatively different mechanisms. Motivated by this hypothesis, we explored four models of morphogenesis — vascular patterning,

diffusion-driven positional information, reaction-diffusion, and random pattern generation — and we have shown that, by acting alone or in concert, they can produce a wide range of flower pigmentation patterns.

The diversity and complexity of these patterns makes it difficult to compare models to nature using objective, quantitative measures. Consequently, we have followed the tradition of visual comparisons of synthetic images with photographs, exemplified by De Gomensoro Malheiros et al. [2020]; Fowler et al. [1992]; Meinhardt [2009]; Owens et al. [2016]; Runions et al. [2005]; Sanderson et al. [2006], and others. In our opinion, many models, including bearberry (Fig. 8), *Mimulus* (Fig. 1), *Kohleria* (Fig. 17), *Trichoglottis* (Fig. 19), and *Phalaenopsis* (Figs. 21 and 23) approximate reality closely. However, the boundaries of pigmented spots in *Primula* (Fig. 10) and dots in foxglove (Fig. 15) seem more irregular in nature than in the models. A stepping stone to understanding and faithfully modeling these irregularities may be microscopic observations of pigmentation patterns, which may reveal their relation to the cellular structure of the petals or to minor veins.

The time to develop the models presented in Section 4 ranged from hours to days. It was longer than using scanned textures, but the result is an insight into the working of nature, gained through the use of visual simulations, in addition to the images themselves. Moreover, once developed, the models can generate many plausible pattern variants (Fig. 15). The time to develop models may decrease as the set of modeled patterns — which may serve as the basis for modeling new ones — grows larger. An intriguing alternative that does not require a deep understanding of the inner workings of the models is the use of evolutionary techniques, in which model parameters and, possibly, the equations themselves, are automatically "mutated", and the modeler guides pattern evolution by selecting preferred outcomes [Risi et al. 2016; Sims 1991].

Several topics are open for further research. General-purpose modeling tools, such as those provided by Blender, make it possible to capture the shape of any flower, but the modeling process is tedious and time-consuming. A specialized flower editor (for instance extending the work of Ijiri et al. [2005] or Owens et al. [2016] to bilaterally symmetric flowers) would offer a more convenient solution. A related issue is the biologically-plausible randomization of flower shapes, reflecting the naturally occurring variations needed to create scenes with many flowers of the same type. A more fundamental extension would be the incorporation of pigmentation patterning into a model of flower development. Growth plays an important role in many instances of pattern formation, such as the patterning of fish skin [Kondo and Asai 1995] and animal coats [De Gomensoro Malheiros et al. 2020], which our simplifying assumption of simulating pattern formation on static flower shapes neglects. In flowers, growth is essential to the development of patterns induced by transposon excision [Rolland-Lagan et al. 2003]. Moreover, patterns that we have reproduced by assuming anisotropic morphogen propagation may in fact be due to anisotropic growth rather than anisotropic diffusion. The incorporation of growth — and the feedback between patterning and growth [Runions et al. 2017] — may provide a path towards explaining the factors we defined as prepatterns in our implementation. In this context, more experimental

results characterizing the development of flower pigmentation patterns in nature are clearly needed. A particularly intriguing question is the formation of reticulate vascular patterns (veins with loops). Although some reticulate patterns have been simulated (e.g., [Runions et al. 2005]), the general problem of modeling venation patterns in flower petals and leaves remains unsolved.

REFERENCES

Chiara A Airoldi, Jordan Ferria, and Beverley J Glover. 2019. The cellular and genetic basis of structural colour in plants. *Current Opinion in Plant Biology* 47 (2019), 81–87.

Nick W Albert, Kevin M Davies, David H Lewis, Huaibi Zhang, Mirco Montefiori, Cyril Brendolise, Murray R Boase, Hanh Ngo, Paula E Jameson, and Kathy E Schwinn. 2014b. A conserved network of transcriptional activators and repressors regulates anthocyanin pigmentation in eudicots. *The Plant Cell* 26 (2014), 962–980.

Nick W Albert, Kevin M Davies, and Kathy E Schwinn. 2014a. Gene regulation networks generate diverse pigmentation patterns in plants. *Plant Signaling & Behavior* 9 (2014), e29526.

Mathieu Andreux, Emanuele Rodola, Mathieu Aubry, and Daniel Cremers. 2015. Anisotropic Laplace-Beltrami operators for shape analysis. In *European Conference on Computer Vision 2014 Workshops, Part IV*, Vol. Lecture Notes in Computer Science 8928. Springer, 299–312.

BlenderNation. 2021. Blender. (2021). https://www.blendernation.com

Mario Botsch, Leif Kobbelt, Mark Pauly, Pierre Alliez, and Bruno Lévy. 2010. *Polygon Mesh Processing*. CRC Press, Boca Raton.

Mikolaj Cieslak, Andrew Owens, and Przemyslaw Prusinkiewicz. 2021. Computational models of auxin-driven patterning in shoots. *Cold Spring Harbor Perspectives in Biology* (2021), a040097.

Robert L Cook. 1984. Shade trees, In Proceedings of ACM SIGGRAPH 1984. *ACM SIGGRAPH Computer Graphics 1984*, 223–231.

Keenan Crane, Fernando de Goes, Mathieu Desbrun, and Peter Schröder. 2013. Digital Geometry Processing with Discrete Exterior Calculus. In *ACM SIGGRAPH 2013 Course Notes*. ACM, New York, NY, USA, 1–126.

Kevin M Davies, Nick W Albert, and Kathy E Schwinn. 2012. From landing lights to mimicry: the molecular regulation of flower colouration and mechanisms for pigmentation patterning. *Functional Plant Biology* 39 (2012), 619–638.

Marcelo De Gomensoro Malheiros, Henrique Fensterseifer, and Marcelo Walter. 2020. The leopard never changes its spots: realistic pigmentation pattern formation by coupling tissue growth with reaction-diffusion. *ACM Transactions on Graphics* 39, 4 (2020), 63:1–13.

Mathieu Desbrun, Eva Kanso, and Yiying Tong. 2006. Discrete differential forms for computational modeling. In *Discrete Differential Geometry: An Applied Introduction (SIGGRAPH 2006 Course Notes)*, Eitan Grinspun (Ed.). 287–324.

Samira M Descombes, Daljit S Dhillon, and Matthias Zwicker. 2015. Optimized CUDA-based PDE solver for reaction diffusion systems on arbitrary surfaces. In *International Conference on Parallel Processing and Applied Mathematics*. 526–536.

Baoqing Ding, Erin L Patterson, Srinidhi V Holalu, Jingjian Li, Grace A Johnson, Lauren E Stanley, Anna B Greenlee, Foen Peng, Harvey D Bradshaw Jr, Michael L Blinov, Benjamin K Blackman, and Yao-Wu Yuan. 2020. Two MYB proteins in a self-organizing activator-inhibitor system produce spotted pigmentation patterns. *Current Biology* 30 (2020), 802–814.

Lance Flavell. 2010. *Beginning Blender: Open Source 3D Modeling, Animation, and Game Design*. Apress / Springer, New York.

Deborah R Fowler, Hans Meinhardt, and Przemyslaw Prusinkiewicz. 1992. Modeling seashells. In *Proceedings of ACM SIGGRAPH 1992*. 379–387.

Atiyo Ghosh, Andre Leier, and Tatiana T Marquez-Lago. 2015. The spatial chemical Langevin equation and reaction diffusion master equations: moments and qualitative solutions. *Theoretical Biology and Medical Modelling* 12 (2015), 1–14.

Alfred Gierer and Hans Meinhardt. 1972. A theory of biological pattern formation. *Kybernetik* 12 (1972), 30–39.

Daniel T Gillespie. 2000. The chemical Langevin equation. *Journal of Chemical Physics* 113 (2000), 297–306.

Daniel T Gillespie. 2007. Stochastic simulation of chemical kinetics. *Annual Review of Physical Chemistry* 58 (2007), 35–55.

Peter Gray and Stephen K Scott. 1984. Autocatalytic reactions in the isothermal, continuous stirred tank reactor: Oscillations and instabilities in the system $A+2B \rightarrow 38; B \rightarrow C$. *Chemical Engineering Science* 39 (1984), 1087–1097.

Amelia A Green, J Richard Kennaway, Andrew I Hanna, J Andrew Bangham, and Enrico Coen. 2010. Genetic control of organ shape and tissue polarity. *PLoS Biology* 8 (2010), e1000537.

Jeremy B A Green and James Sharpe. 2015. Positional information and reaction-diffusion: Two big ideas in developmental biology combine. *Development* 142, 7 (2015), 1203–1211.

Erich Grotewold. 2006. The genetics and biochemistry of floral pigments. *The Annual Revue of Plant Biology* 57 (2006), 761–780.

Torsten Hädrich, Bedrich Benes, Oliver Deussen, and Sören Pirk. 2017. Interactive modeling and authoring of climbing plants. *Computer Graphics Forum* 36, 2 (2017), 49–61.

Pat Hanrahan and Paul Haeberli. 1990. Direct WYSIWYG painting and texturing on 3D shapes. *ACM SIGGRAPH Computer Graphics* 24 (1990), 215–223.

Takashi Ijiri, Shigeru Owada, Makoto Okabe, and Takeo Igarashi. 2005. Floral diagrams and inflorescences: interactive flower modeling using botanical structural constraints. In *Proceedings of ACM SIGGRAPH 2005*. 720–726.

Takashi Ijiri, Shin Yoshizawa, Hideo Yokota, and Takeo Igarashi. 2014. Flower modeling via X-ray computed tomography. *ACM Transactions on Graphics* 33 (2014), 48:1–10.

Wenzel Jakob. 2021. Instant Meshes. (2021). https://github.com/wjakob/instant-meshes

Wenzel Jakob, Marco Tarini, Daniele Panozzo, and Olga Sorkine-Hornung. 2015. Instant field-aligned meshes. *ACM Transactions on Graphics* 34 (2015), 189:1–15.

Radoslaw Karwowski and Przemyslaw Prusinkiewicz. 2003. Design and implementation of the L+C modeling language. In *Electronic Notes in Theoretical Computer Science*, Vol. 86. 134–152.

Richard Kennaway, Enrico Coen, Amelia Green, and Andrew Bangham. 2011. Generation of diverse biological forms through combinatorial interactions between tissue polarity and growth. *PLoS Computational Biology* 7 (2011), e1002071:1–22.

Shigeru Kondo and Rihito Asai. 1995. A reaction–diffusion wave on the skin of the marine angelfish *Pomacanthus*. *Nature* 376 (1995), 765–768.

Peter A Lawrence. 1992. *The Making of a Fly: The Genetics of Animal Design*. Blackwell Scientific Publications, Oxford.

David W Lee. 2010. *Nature's Palette: the Science of Plant Color*. University of Chicago Press.

Kyoung J Lee, W D McCormick, Qi Ouyang, and Harry L Swinney. 1993. Pattern formation by interacting chemical fronts. *Science* 261 (1993), 192–194.

Ling Lu and Wenlin Song. 2014. Simulation research for petal color. *Applied Mechanics and Materials* 667 (2014), 237–241.

Claudio Mancinelli, Marco Livesu, and Enrico Puppo. 2019. A comparison of methods for gradient field estimation on simplicial meshes. *Computers & Graphics* 80 (2019), 37–50.

Hans Meinhardt. 1982. *Models of Biological Pattern Formation*. Academic Press, London.

Hans Meinhardt. 2009. *The Algorithmic Beauty of Sea Shells. Fourth Edition*. Springer, Dordrecht.

Mark Meyer, Mathieu Desbrun, Peter Schröder, and Alan H Barr. 2003. Discrete differential-geometry operators for triangulated 2-manifolds. In *Visualization and Mathematics III*, Polthier K. Hege HC. (Ed.). Springer, Berlin, 35–57.

Andrew Owens, Mikolaj Cieslak, Jeremy Hart, Regine Classen-Bockhoff, and Przemyslaw Prusinkiewicz. 2016. Modeling dense inflorescences. *ACM Transactions on Graphics* 35, 4 (2016), 136:1–14.

John E Pearson. 1993. Complex patterns in a simple system. *Science* 261 (1993), 189–192.

Ken Perlin. 1985. An image synthesizer. *ACM Siggraph Computer Graphics* 19, 3 (1985), 287–296.

Przemyslaw Prusinkiewicz, Mark S Hammel, and Eric Mjolsness. 1993. Animation of plant development. *Proceedings of ACM SIGGRAPH 1993* (1993), 351–360.

Przemyslaw Prusinkiewicz and Aristid Lindenmayer. 1990. *The Algorithmic Beauty of Plants*. Springer, New York. With contributions by James S. Hanan, F. David Fracchia, Deborah R. Fowler, Martin J. M. de Boer and Lynn Mercer.

Przemyslaw Prusinkiewicz, Lars Mündermann, Radoslaw Karwowski, and Brendan Lane. 2001. The use of positional information in the modeling of plants. In *Proceedings of ACM SIGGRAPH 2001*. 289–300.

Lee Ringham. 2020. *Modelling Natural Phenomenon with Reaction-Diffusion*. Master's thesis. University of Calgary.

Lee Ringham, Przemyslaw Prusinkiewicz, and Robert Gniadecki. 2019. Skin patterning in psoriasis by spatial interactions between pathogenic cytokines. *iScience* 20 (2019), 546–553.

Sebastian Risi, Joel Lehman, David B D'Ambrosio, Ryan Hall, and Kenneth O Stanley. 2016. Petalz: Search-based procedural content generation for the casual gamer. *IEEE Transactions on Computational Intelligence and AI in Games* 8, 3 (2016), 244–255.

Yodthong Rodkaew, Suchada Siripant, Chidchanok Lursinsap, and Prabhas Chongstitvatana. 2002. An algorithm for generating vein images for realistic modeling of a leaf. In *Proceedings of Computational Mathematics and Modeling 2002*. 1–9.

Anne-Gaëlle Rolland-Lagan, J Andrew Bangham, and Enrico Coen. 2003. Growth dynamics underlying petal shape and asymmetry. *Nature* 422 (2003), 161–163.

Sheldon M Ross. 1997. *Introduction to Probability Models*. Academi Press.

Adam Runions, Martin Fuhrer, Brendan Lane, Pavol Federl, Anne-Gaëlle Rolland-Lagan, and Przemyslaw Prusinkiewicz. 2005. Modeling and visualization of leaf venation patterns. In *Proceedings of ACM SIGGRAPH 2005*. 702–711.

Adam Runions, Miltos Tsiantis, and Przemyslaw Prusinkiewicz. 2017. A common developmental program can produce diverse leaf shapes. *New Phytologist* 216 (2017), 401–418.

Tsvi Sachs. 2003. Collective specification of cellular development. *BioEssays* 25, 9 (2003), 897–903.

Allen R Sanderson, Robert M Kirby, Chris R Johnson, and Lingfa Yang. 2006. Advanced reaction-diffusion models for texture synthesis. *Journal of Graphics Tools* 11 (2006), 47–71.

Kathy Schwinn, Julien Venail, Yongjin Shang, Steve Mackay, Vibeke Alm, Eugenio Butelli, Ryan Oyama, Paul Bailey, Kevin Davies, and Cathie Martin. 2006. A small family of MYB-regulatory genes controls floral pigmentation intensity and patterning in the genus *Antirrhinum*. *The Plant Cell* 18 (2006), 831–851.

Yongjin Shang, Julien Venail, Steve Mackay, Paul C Bailey, Kathy E Schwinn, Paula E Jameson, Cathie R Martin, and Kevin M Davies. 2011. The molecular basis for venation patterning of pigmentation and its effect on pollinator attraction in flowers of *Antirrhinum*. *New Phytologist* 189 (2011), 602–615.

Karl Sims. 1991. Artificial evolution for computer graphics. In *Proceedings of ACM SIGGRAPH 1991*. 319–328.

Andrew Sugden. 1984. *Longman Illustrated Dictionary of Botany*. Longman, Burnt Mill.

Kazuma Suzuki, Tomohiro Suzuki, Takashi Nakatsuka, Hideo Dohra, Masumi Yamagishi, Kohei Matsuyama, and Hideyuki Matsuura. 2016. RNA-seq-based evaluation of bicolor tepal pigmentation in Asiatic hybrid lilies *Lilium spp.*. *BMC Genomics* 17 (2016), 1–19.

Alan Turing. 1952. The chemical basis of morphogenesis. *Philosophical Transactions of the royal Society B* 237 (1952), 37–72.

Greg Turk. 1991. Generating textures on arbitrary surfaces using reaction-diffusion. *Proceedings of ACM SIGGRAPH 1991* (1991), 289–298.

Casper J van der Kooi, J Theo M Elzenga, Marten Staal, and Doekele G Stavenga. 2016. How to colour a flower: on the optical principles of flower coloration. *Proceedings of the Royal Society B: Biological Sciences* 283 (2016), 20160429:1–9.

Casper J van der Kooi, Bodo D Wilts, Hein L Leertouwer, Marten Staal, J Theo M Elzenga, and Doekele G Stavenga. 2014. Iridescent flowers? Contribution of surface structures to optical signaling. *New Phytologist* 203 (2014), 667–673.

John A Vastano, John E Pearson, W Horsthemke, and Harry L Swinney. 1987. Chemical pattern formation with equal diffusion coefficients. *Physics Letters A* 124 (1987), 320–324.

Pat Willmer. 2011. *Pollination and Floral Ecology*. Princeton University Press, Princeton.

Edwin B Wilson and Josiah W Gibbs. 1901. *Vector Analysis: a text-book for the use of students of mathematics and physics founded upon the lectures of J. Willard Gibbs*. Yale University Press, New Haven.

Andrew Witkin and Michael Kass. 1991. Reaction-diffusion textures. In *Proceedings of ACM SIGGRAPH 1991*. 299–308.

Lewis Wolpert. 1969. Positional information and the spatial pattern of cellular differentiation. *Journal of Theoretical Biology* 25, 1 (1969), 1–47.

Masumi Yamagishi. 2013. How genes paint lily flowers: Regulation of colouration and pigmentation patterning. *Scientia Horticulturae* 163 (2013), 27–36.

Lidia Yamamoto, Daniele Miorandi, Pierre Collet, and Wolfgang Banzhaf. 2011. Recovery properties of distributed cluster head election using reaction–diffusion. *Swarm Intelligence* 5 (2011), 225–255.

Yao-Wu Yuan. 2019. Monkeyflowers (*Mimulus*): new model for plant developmental genetics and evo-devo. *New Phytologist* 222 (2019), 694–700.

Yao-Wu Yuan, Alexandra B Rebocho, Janelle M Sagawa, Lauren E Stanley, and Harvey D Bradshaw. 2016. Competition between anthocyanin and flavonol biosynthesis produces spatial pattern variation of floral pigments between *Mimulus* species. *Proceedings of the National Academy of Sciences* 113 (2016), 2448–2453.

Yao-Wu Yuan, Janelle M Sagawa, Laura Frost, James P Vela, and Harvey D Bradshaw Jr. 2014. Transcriptional control of floral anthocyanin pigmentation in monkeyflowers (*Mimulus*). *New Phytologist* 204 (2014), 1013–1027.

Chenxi Zhang, Mao Ye, Bo Fu, and Ruigang Yang. 2014. Data-driven flower petal modeling with botany priors. In *Proceedings of the IEEE Conference on Computer Vision and Pattern Recognition*. 636–643.

Ning Zhou, Weiming Dong, Jiaxin Wang, and Jean-Claude Paul. 2007. Modeling and visualization of flower color patterns. In *10th IEEE International Conference on Computer-Aided Design and Computer Graphics*. 150–155.